https://doi.org/10.5194/essd-2025-427
Preprint. Discussion started: 27 December 2025

Open Access Earth System Science Data Discussions

China Open Biomass Burning Emissions Inventory (COBBEI) from 2020 to 2023: Multi-Satellite Fusion via FRP-Based Filtering Rules

Jingwen Shi[1,2], Yaqin Ji[1,2], Wenju Xu[1,2], Ruixing Shen[1,2], Jiaofan Ma[1,2], Yuexin Zhao[1,2], Xingchen Zhou[1,2], Yushang Ma[1,2], Yinchang Feng[1,2]

[1]College of Environmental Science and Engineering, Nankai University, Tianjin, 300350, China
[2]State Environmental Protection Key Laboratory of Urban Ambient Air Particulate Matter Pollution Prevention and Control, Tianjin, 300350, China

Correspondence to: Yaqin Ji (jiyaqin@nankai.edu.cn)

Abstract: Pollutants released from open biomass burning (OBB) considerably impact air quality, human health, and ecosystems. Only a few studies have used geostationary satellites to monitor OBB emissions in China. Therefore, we construct the China Open Biomass Burning Emissions Inventory (COBBEI) from 2020 to 2023. This dataset included eight pollutants with a temporal resolution of 1 hour and a spatial resolution of 2 km. The COBBEI integrated multi-satellite data, including MODIS, NPP, and Fengyun-4A (FY-4A). The Fire Radiation Power (FRP) data were reconstructed to the FRP cycle, and we integrated the curves to obtain the hourly biomass burned. We also developed five filtering rules based on FRP, considering fire point frequency, radiation values, timing, and variation. These rules were applied to correct the land cover maps, and their validity was verified. The annual average emissions of CO_2, CO, CH_4, NO_x, SO_2, $PM_{2.5}$, K, and LG were 46530, 2262, 132, 82, 25, 247, 11, and 12 Gg, respectively. The spatial distribution characteristics of all eight pollutants were generally consistent. Northeast China served as a major center of pollutant emissions. Different types of fires exhibited various spatial distributions. By validating the method and comparing it with other databases, it was confirmed that COBBEI reduced uncertainty in the OBB emission inventory by providing more information on fire points and effectively screening out fires that were not from OBB. The dataset could offer essential data for air quality modeling, environmental policy development, and fire emergency response strategies. The COBBEI dataset can be downloaded at https://figshare.com (last access: 2025-06-20) with the following DOI: https://doi.org/10.6084/m9.figshare.29367869.v1(Shi and Ji, 2025).

1. Introduction

Open biomass burning (OBB) refers to the combustion of biomass occurring in open environments, including cropland fires, forest fires, grassland fires, and other wildfires. The combustion of OBB consistently releases significant air pollutants (Urbanski et al., 2008), which include carbon compounds (e.g., CO_2, CO, CH_4), nitrogen oxides (e.g., NO_2), sulfur compounds (e.g., SO_2), and particulate matter (e.g., $PM_{2.5}$). In particular, certain unique tracers, such as levoglucosan (LG) and potassium (K), have been widely adopted as diagnostic markers for identifying the source of pollutants (Khan et al., 2021). However, the

https://doi.org/10.5194/essd-2025-427
Preprint. Discussion started: 27 December 2025

limited study of these key chemical tracers in OBB emission inventories may introduce significant uncertainties in quantifying and characterizing OBB emissions.

Pollutants emitted from OBB deeply impact local air quality and pose serious risks to human health and ecosystems (Burke et al., 2020; Casey et al., 2024; Molitor et al., 2023; Xue et al., 2021, 2023; Ye et al., 2022). In Northern China, $PM_{2.5}$ source apportionment results indicated that biomass burning ranked as the second-largest contributor, accounting for 19.3%, surpassing vehicle exhaust emissions (Zong et al., 2016). During the harvest season in the Yangtze River Delta, its contribution reached as high as 37% (Cheng et al., 2014). Beyond particles, OBB releases hazardous organic compounds, including polycyclic aromatic hydrocarbons (PAHs) and their derivatives, further exacerbating air pollution (Aguilera et al., 2021; Ravindra et al., 2008). Growing evidence suggests that these emissions contribute to substantial adverse health outcomes. Inhaling PAHs from wildfire smoke increased both cancer and non-cancer risks. This risk existed whether exposure happens indoors or outdoors, even over a short period (Ghetu et al., 2022). Long-term exposure to wildfire smoke may also increase the risk of lung cancer and brain tumors (Korsiak et al., 2022). Therefore, accurate estimation of pollutant emissions is crucial as it supports air quality models (Reid et al., 2009), informs environmental policy planning, protects public health, and helps build a more sustainable future (Zhou et al., 2017).

The spatial and temporal distribution characteristics of pollutants from OBB in China exhibit variations across different periods. Ning et al. (2024) found that the number of fire points reached their peak in 2010, decreased steadily until 2017, and then began to rise slowly. An empirical study (Yang et al., 2020) on straw burning management in Northeast China found that after implementing mandatory straw burning bans in Heilongjiang and Jilin provinces in 2018, $PM_{2.5}$ emissions in 2018 from OBB during the harvest period decreased by 48.1% compared to 2015. However, due to the time lag in emission inventories (Jiang et al., 2024; Wooster et al., 2021), research on OBB emission data after 2022 remains limited. At the same time, Ke et al.(2019) compared average temperatures and precipitation in Northeast and North China from 2013 to 2017 and found that the area burned was positively correlated with average temperature and negatively correlated with average precipitation. Shabbir et al. (2023) pointed out that OBB emissions in China may become more frequent with climate change through prediction. Therefore, there is a need for timely satellite-based research on OBB emission inventories in China.

Active fire remote sensing is critical for providing timely and accurate fire activity information (Wooster et al., 2021). Up to now, there are two active fire monitoring methods to calculate the emission from OBB. The method based on burned area (BA) has been widely employed in local and global OBB databases such as GFED (van der Werf et al., 2017), FINN (Wiedinmyer et al., 2011), the study by Qiu et al.(2016), and GEIOBB (Liu et al., 2024). However, since the BA method makes it difficult

https://doi.org/10.5194/essd-2025-427
Preprint. Discussion started: 27 December 2025

to determine the combustion efficiency of fires, preset parameters were used to represent incomplete combustion and biomass per unit area. This introduces significant uncertainties. While the BA method shows high accuracy for larger and more compact burned patches, the preset parameters may lead to overestimated emissions for small-scale fires (SFs). With the increasing frequency of SFs in China (Xu et al., 2023), using the BA method for emission calculations could introduce substantial uncertainties. Unlike the BA method, Fire Radiated Power (FRP) could compensate for the shortcomings of BA. This method uses the direct linear relationship between FRP integration and biomass burned to calculate the pollutants emitted by OBB. This method typically relies on Wooster's total dry matter (i.e., biomass burned) formula (2005) as a theoretical framework. Therefore, the temporal resolution of emission inventories can be increased daily or even hourly (Li et al., 2022).

The effectiveness of the FRP method largely depends on the spatial and temporal resolution of satellite observations. When relying solely on polar orbit satellites, their orbital characteristics and temporal gaps limit the ability to provide continuous and accurate FRP data (Li et al., 2022). Most FRP-based emission inventories that only use polar orbit satellites rely on field surveys and predefined Gaussian functions to reconstruct the entire FRP cycle from limited FRP values (Wu et al., 2021; Zhao et al., 2021). Errors have been observed in the timing of peak emissions and the hourly distribution of fires (Mota and Wooster, 2018; Ye et al., 2021). Geostationary satellites can provide more coherent data to reconstruct FRP cycles. Therefore, integrating geostationary and polar orbit satellites offers a promising solution for enhancing both the temporal and spatial resolution of emission inventories (Li et al., 2019; Xu, 2021). For example, Li et al. (2019) fused FRP retrievals from the Geostationary Operational Environmental Satellite (GOES) with data from the MODIS Collection 6. Similarly, Xu et al. (2023) fused data from the Himawari-8 geostationary satellite with two polar orbit satellites to reconstruct the FRP cycle hourly. Studies utilizing Chinese geostationary satellites for OBB monitoring remain scarce.

The launch of FY-4A in 2019 made it possible to calculate China's OBB emission inventory using the combination of data from the Chinese geostationary satellite and international polar orbit satellites. Therefore, this study aims to: 1. Establish the China Open Biomass Burning Emissions Inventory (COBBEI) from 2020 to 2023 based on FY-4A and two datasets from polar orbit satellites. 2. Analyze the spatiotemporal distribution characteristics of COBBEI at hourly scales to reveal dynamic patterns and regional variations. 3. Propose five filtering rules derived from the inventory data and validate their reliability through comparative analysis.

2 Methods

Based on previous studies (Vermote et al., 2009; Xu et al., 2022), the data processing consisted of four steps: pre-processing, spatial fusion, temporal fusion, and final computation (Fig.1).

https://doi.org/10.5194/essd-2025-427
Preprint. Discussion started: 27 December 2025

Open Access Earth System Science Data Discussions

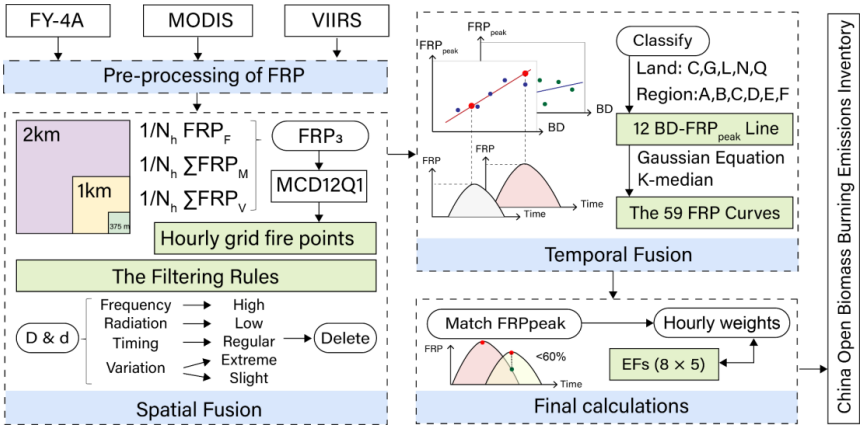

Figure 1: The research framework in this study.

The spatial fusion process involved integrating hourly grid fire points and filtering rules. Temporal fusion encompassed fire classification, fitting the linear relationship between the maximum FRP (FRP_{peak}) and burning duration (BD), and reconstructing FRP curves. The final calculations included peak matching, hourly weight calculation, and the organization of emission factors (EFs). The details of the four steps are as follows.

2.1 Dataset and scopes

The high spatial resolution FRP data were obtained from MODIS/Aqua Terra Thermal Anomalies/Fire locations 1km FIRMS NRT (LANCEMODIS, 2021) and VIIRS (NOAA-20/JPSS-1) I Band 375 m Active Fire Product NRT (The Visible Infrared Imaging Radiometer Suite) (NASA VIIRS Land Science Team, 2020). These two datasets from polar orbit satellites are commonly used in OBB emission datasets (Ferrada et al., 2022; Wiedinmyer et al., 2023; Zhao et al., 2021). The geostationary satellite FRP data were obtained from FY-4A AGRI L2 Fire/Hot spot detection product (FHS) (National Satellite Meteorological Center, 2024), collected by the Advanced Geosynchronous Radiation Imager (AGRI). The land cover data were from MCD12Q1 (Friedl and Sulla-Menashe, 2022), created from the Terra and Aqua satellites. More detailed information about the dataset was available in the supplementary materials.

The COBBEI spanned from 2020 to 2023, and this study focused on mainland China, encompassing 31 provinces while excluding Hong Kong, Macao, and Taiwan. The dataset included CO_2, CO, CH_4, $PM_{2.5}$, Potassium (K), SO_2, NO_x, and Levoglucosan (LG), with a temporal resolution of 1 hour and a spatial resolution of 2 km.

2.2 Pre-processing of FRP

Fusing data from three datasets with different resolutions required pre-processing steps. Fire points with low confidence were excluded based on the following criteria: MODIS data with the CONFIDENCE value below 20, VIIRS data marked as

https://doi.org/10.5194/essd-2025-427
Preprint. Discussion started: 27 December 2025

'LOW'(Xu et al., 2022), and FY-4A data with the RELIABILITY score less than 2. Next, the fire points were converted into a 2 km × 2km grid based on the latitude and longitude coordinates. At last, the land cover maps were applied to exclude fire points located in land cover types 13 (urban and built-up lands), 15 (permanent snow and ice), 16 (barren or sparsely vegetated), and 17 (water bodies).

2.3 Spatial fusion

Spatial fusion required the formation of hourly grid fire points first. The data from different satellites must be fused at the same resolution and produce representative hourly grid fire points in the same hour. The established fusion formula (S1) was shown in the supplement material.

Subsequently, some anomalous fire points were found in the calculations, so we developed five filtering rules to remove those not from OBB. The flowchart was shown in Fig.2. First, we needed to exclude fire points originating from wetlands (land cover value = 11). Wetland fires generally exhibited low radiant power due to their high biomass and moisture content (Peng et al., 2022; Wooster et al., 2021), making them easily confused with ground radiation or anthropogenic heat sources. Therefore, wetland fire points were retained directly. Then, we calculated the total number of fire days (D) and the highest number of consecutive fire days (d) in each month for each grid. The fire points were filtered based on the following criteria.

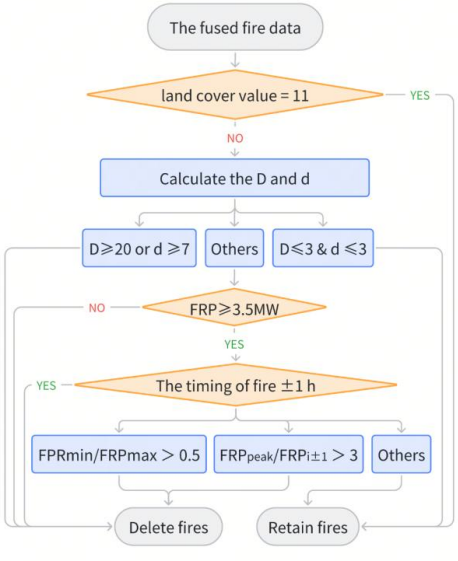

Figure 2: The flowchart of five filtering rules

1. **Frequency:**

Reason: Andela et al. (2019) found that the average duration of OBB was less than 20 days, and a single fire was typically under 7 days. Grids with a high frequency of consecutive fires usually had other heat sources.

https://doi.org/10.5194/essd-2025-427
Preprint. Discussion started: 27 December 2025

Operation: Exclude fire points with high frequency. Delete fire points where D > 20 or d > 7. Retain fire points where both D and d are < 3.

2. **Radiation values:**

Reason: Due to their natural heat or the sunlight, some areas may produce ground radiation with much lower radiation power than OBB. These needed to be excluded to avoid interference.

Operation: Exclude fire points with low radiation power over a long time. Delete fire points with FRP ≤ 3.5MW in the left data.

3. **Timing:**

Reason: The fire points from OBB usually do not have temporal consistency. In contrast, artificial activities like coal-fired power plants or blast furnace steel plants have regular timing. These data should be excluded.

Operation: Exclude fire points from man-made activity. Remove fire points where the daily fire start time was always within ±1 hour of other fires in the left data.

4. **Variation (1):**

Reason: The FRP of fire from OBB typically has a gradual, single-peak distribution(Vermote et al., 2009), whereas industrial activities or cloud interference could produce sudden spikes in radiation power. These extreme values should be excluded.

Operation: Exclude fire points that had instantaneous extreme values. Delete fire points where FRP_{peak} exceeds more than three times the FRP within an hour before or after the timing ($FRP_{i\pm1}$).

5. **Variation (2):**

Reason: Low-volatile fire points, where the FRP shows a slight variation, do not match the expected characteristics of the FRP from OBB.

Operation: Exclude fire points with low volatility. Remove fire points where the ratio of the minimum FRP (FRP_{min}) to FRP_{max} is greater than 0.5.

Previous studies often used land cover maps to differentiate data and estimated the likely fuel type (Schollaert et al., 2024). However, even land cover maps with the highest spatial resolution typically apply the ">60% coverage" criterion when defining grid values (Sulla-Menashe and Friedl, 2018). Furthermore, the temporal resolution of land cover maps was usually limited to one year. The spatial and temporal variations could particularly affect areas along the interface between urban and wildland zones (WUI). These filtering rules we developed would improve the accuracy of the OBB emission inventory based on the FRP characteristics.

https://doi.org/10.5194/essd-2025-427
Preprint. Discussion started: 27 December 2025

2.4 Temporal fusion

2.4.1 Fire classification

The fire points were classified into five fire types: C (evergreen forest), L (deciduous forest), G (grasslands), N (croplands), and Q (other types) for simplified calculation. During the initial investigation, we applied the least squares method to fit the best curves for the FRP of individual fires across different land cover and provinces. Six single-peaked curve models were considered for this process: Laplace, Weibull, Gaussian, lognormal, and beta curves. Each fire type was further divided into several regions based on the proportion of the optimal curve and different environmental factors. Cropland fires were divided based on the proportion of crop cultivation in each province. Grassland fires were divided based on altitude, and evergreen forest fires were divided based on the climatic differences between northern and southern China. The deciduous forest fire and other types of fires were not divided. The fire points from different fire types were divided into 12 regions, as detailed in Fig.3.

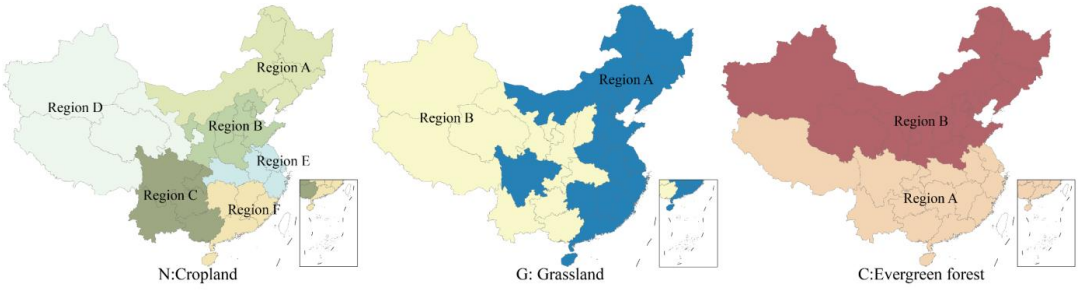

Figure 3: Region classification for different types of fires in China.

2.4.2 Burning duration

The relationship between BD and FRP_{peak} follows a linear pattern (Xu et al., 2022), and the formula is shown in the supplement material. The fitting results are shown in Fig.4 and Table S1, and the revised R^2 ranged from 0.53 to 0.95. The results indicated that the FRP values generated by the burning of agricultural residue in Northeast China were higher than those of other types of fires. Additionally, grassland fires in flat areas could last longer. There were apparent linear differences in fire characteristics between different fire types and regions.

https://doi.org/10.5194/essd-2025-427
Preprint. Discussion started: 27 December 2025

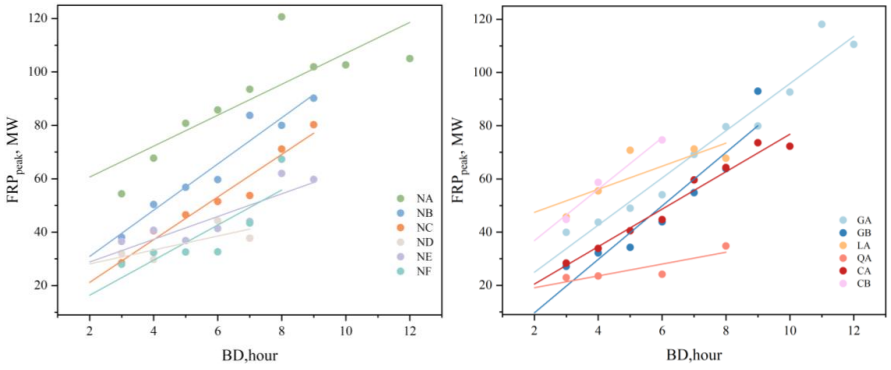

Figure 4: Regression models between BD and FRP$_{peak}$ for different land cover data in different regions.

2.4.3 FRP cycle reconstruction models

When the BD of fires is shorter than 4 hours, it is difficult to analyze the patterns through limited hourly FRP data (Vermote et al., 2009). In other words, when satellite monitoring data for a fire point exceeds 4 hours, we could restore the FRP curve by fitting parameters through a curve model. Initial investigation revealed that Gaussian functions might best fit most FRP cycles in all fire types, which aligns with previous studies (Liu et al., 2015; Yang and Zhao, 2019). The parameters $\boldsymbol{\alpha}$ and $\boldsymbol{\kappa}$ by different BD and fire types were obtained in the Gaussian Eq.(1).

$$FRP(\mathrm{h}) = FRP_{peak} \cdot \exp\left(-\frac{1}{2}\left(\frac{\mathrm{h}-\alpha}{\kappa}\right)^2\right) \quad \textbf{(1)}$$

Throughout this essay, $\boldsymbol{h}$ means the timing; $\boldsymbol{\alpha}$ and $\boldsymbol{\kappa}$ are parameters that need to be fitted.

Considering the potential noise and extreme values, the k-median clustering algorithm was applied to integrate the global best-fit parameters (Fig.S1). 59 curve models were obtained and shown in Fig.5 and Table S2. They corresponded well with the BD. For fires shorter than 4 hours, we used Gaussian function parameters ($\boldsymbol{\alpha}$ was set as BD/2, and $\boldsymbol{\kappa}$ as BD/4) based on related literature (Vermote et al., 2009).

Based on Wooster's formula(2005), we integrated the fitted curves and assigned hourly weights to the integrals based on the time of the maximum fire value. The formula is given in Eq.(2).

$$E_{h,c} = \beta \times \int \mathrm{FRP}(\mathrm{BD}, \mathrm{Land}, \mathrm{Region})\mathrm{dt} \times FRP_{peak} \times EF_{c,L} \quad \textbf{(2)}$$

Where $\boldsymbol{E}$ represents the emission from OBB; $\mathbf{c}$ represents the type of compounds; $\boldsymbol{\beta}$ represents the combustion factor, 0.41 kg/MJ (Freeborn et al., 2014); $\boldsymbol{FRP(BD, Land, Region)}$ represents FRP curves corresponding to different durations, fire types, and regions; $\boldsymbol{L}$ represents the land cover data; Throughout this essay, $\boldsymbol{EF}$ means the emission factors.

https://doi.org/10.5194/essd-2025-427
Preprint. Discussion started: 27 December 2025

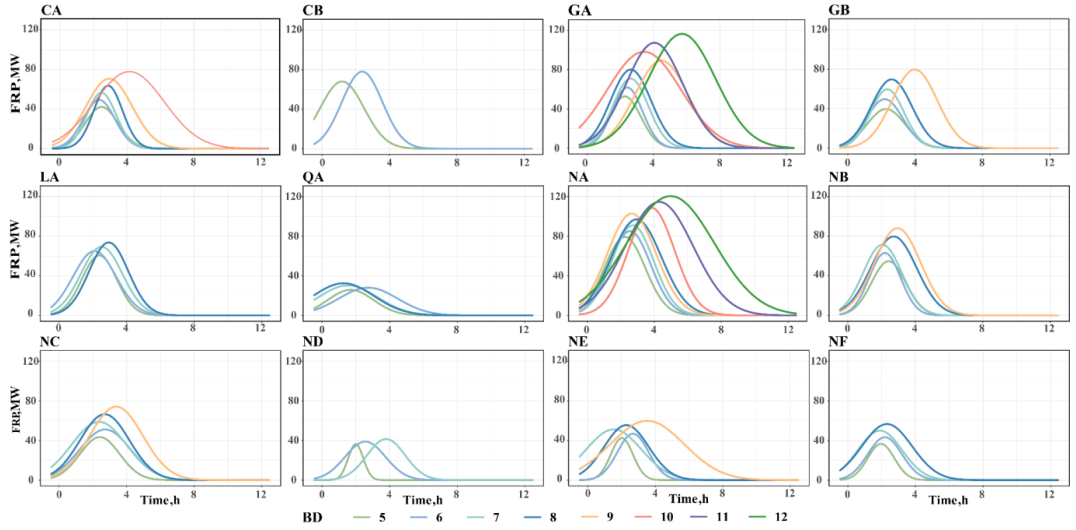

Figure 5: Fitting models for the FRP cycle across 12 land cover types and regions.

It was typical for the FRP_{peak} of two fires to be closely connected. To accurately determine whether these peaks originated from the same fire, this study followed the method of Xu et al. (2023). The time t_2 was taken as the second peak, and inserted into the curve fitted for the first peak. This gave us a reference value. If the relative difference between FRP_{peak2} and FRP_R exceeds 60 %, then the two peaks represented two separate fire events. If the difference between the two peaks was less than 60%, they were considered to originate from the same fire event, and the second peak was deleted.

2.5 Emission factors

EFs indicate the mass of pollutants emitted per unit of total dry matter burned. Previous studies have explored EFs through field (Wiggins et al., 2021), data inversion (Xu et al., 2022), and laboratory measurements (Simões Amaral et al., 2016). These methods showed some variations in the data. We reviewed EFs from the past ten years and observed noticeable differences (Table S3). The most representative values are similar to the average values from previous studies (Binte Shahid et al., 2024). In addition, considering the variability of EF values, the study obtained the EFs by calculating the median values (Table 1).

Table 1: Emission factors for eight types of compounds in five different land cover maps (Unit: g/kg).

Land cover	CO_2	CO	CH_4	NO_x	SO_2	$PM_{2.5}$	K	LG
C	1625.000	97.000	4.680	2.550	0.700	9.900	0.305	0.420
G	1662.500	69.000	2.530	3.465	0.655	6.935	0.315	0.050
L	1550.000	121.000	5.200	1.210	0.850	15.300	0.170	1.315
N	1513.000	76.000	5.820	2.400	1.025	8.200	0.480	0.610
Q	1619.500	225.000	9.100	1.810	1.400	17.000	0.004	0.570

https://doi.org/10.5194/essd-2025-427
Preprint. Discussion started: 27 December 2025

3. Results and discussion

3.1 Temporal distribution

The COBBEI estimated emissions of eight air pollutants which was shown in Fig.6 and Table S4. The annual average emissions of CO_2, CO, CH_4, NO_x, SO_2, $PM_{2.5}$, K, and LG were 46530, 2262, 132, 82, 25, 247, 11, and 12 Gg, respectively. During four years, eight pollutants exhibited three distinct interannual patterns. The total annual CO_2, CO, NO_x, and $PM_{2.5}$ emissions increased yearly. In contrast, CH_4, SO_2, and LG emissions followed a V-shaped trend, slightly declining in 2021. The annual emissions of K fluctuated throughout four years.

3.1.1 The turnarounds with the emissions of certain pollutants in 2021

These turnarounds in emissions of certain pollutants in 2021 were directly related to the decreased burning biomass of agricultural residue this year (Table S5) and EFs of cropland fires.

In 2021, cropland fires were the only type that saw a decline in biomass burned, dropping by 14.7%. Its share of the total biomass burned also declined from 60.3% in 2020 to 50.8% in 2021. The provinces with the most considerable decreases in agricultural burned biomass were Inner Mongolia (56%), Liaoning (42%), and Jilin (31%) compared to 2020. The declines in these provinces could be attributed to local straws burning ban measures and the comprehensive utilization of straw. For instance, Jilin province implemented a three-year action plan from 2019 to 2021, increasing the rate of biomass utilization. The utilization rate of straw in 2021 increased by 13% compared to 2018, although it was still below the national average(Li et al., 2024). This plan helped reduce agricultural residue burning in 2021 and contributed to a continued decline in pollutant emissions across the province over the next two years.

According to the relationship between EFs and emissions, larger EFs resulted in greater sensitivity, where small changes in activity levels could lead to more significant changes in emissions. Notably, for CH_4, SO_2, LG, and K, croplands exhibited the highest or second-highest EFs among all land cover typies. Therefore, emissions of these four pollutants showed a marked decline with the reductions in cropland fires in 2021. Conversely, CO_2, CO, NO_x, and $PM_{2.5}$ emissions exhibited an opposing trend, with sustained increases observed in 2021.

3.1.2 The rise in burned biomass from all fire types in 2022

After annual emissions of some pollutants experienced a turnaround in 2021, the emissions from OBB in China rose sharply in 2022. While the year-on-year growth rates for $PM_{2.5}$ peaked in 2023 at 25.94% (up from 24.10% in 2022), the other seven pollutants all reached their highest growth rates in 2022, ranging between 22.00% and 23.52%. This increase in 2022 was closely linked to the rise in burned biomass from all fire types, particularly the increase in biomass burmed from grassland

https://doi.org/10.5194/essd-2025-427
Preprint. Discussion started: 27 December 2025

fires in October 2022 and the rebound in biomass burnedfrom cropland residue. This indicated the lack of long-term effects from relevant policies and the impact of global climate change on OBB.

In 2020, China introduced an action plan to reach carbon peaking by 2030. Following this, each province developed local action plans to manage agricultural residues. For example, Tianjin carried out "Tianjin Carbon Peak Carbon Neutral Promotion Regulations" from 2021, including promoting the comprehensive utilization of crop straw and supporting the development of non-fossil energy sources such as wind, solar, geothermal, biomass, etc. Regarding air pollution control, some studies have started quantitative evaluations of local straw-burning ban effectiveness. For example, Yang et al. (2020) pointed out that the straw burning ban introduced in 2018 in northeastern China led to a 48.1% reduction in $PM_{2.5}$ concentrations during the post-harvest season compared to 2015. However, a few studies evaluated the long-term effects of these measures. The rebound in agricultural burned biomass in 2022 raised concerns about the lack of sustained impact. For instance, agricultural burned biomass in Inner Mongolia increased by 65% in 2022, after having decreased by 56% in 2021. This phenomenon highlights the need for sustained measures and efforts. The shift from a straightforward total ban on burning to a more balanced approach involving regulation and management calls for authorities to refine local straw measures.

Alternatively, the extreme weather conditions prevalent during 2022 could represent a contributing factor. The average temperature in 2022 was the second highest since 1951, just 0.02°C lower than in 2021. The national average number of high-temperature days (daily maximum temperature ≥35.0°C) reached a record high, 1.8 times the normal level. Compared to the relatively wet conditions in 2021, annual precipitation in 2022 decreased by 10%, marking the driest year recorded since 2012 (China Meteorological Administration, 2023). The climate would continue the warm and dry trend of 2022 in the future. Climate change has significantly affected the size, extent, and frequency of OBB worldwide (Synolakis and Karagiannis, 2024). Specifically, declines in summer precipitation and fewer rain days served as primary drivers of increased wildfire BA(Jones et al., 2022). Precipitation during the fire season exerts the strongest control on BA, directly through its wetting effects and indirectly through feedback to vapor pressure deficit (Holden et al., 2018). Consequently, as global warming intensifies and regional extreme drought events become more frequent(Piedrahita et al., 2024), the risk of pollutant emissions from OBB will grow increasingly complex (Yuan et al., 2022).

https://doi.org/10.5194/essd-2025-427
Preprint. Discussion started: 27 December 2025

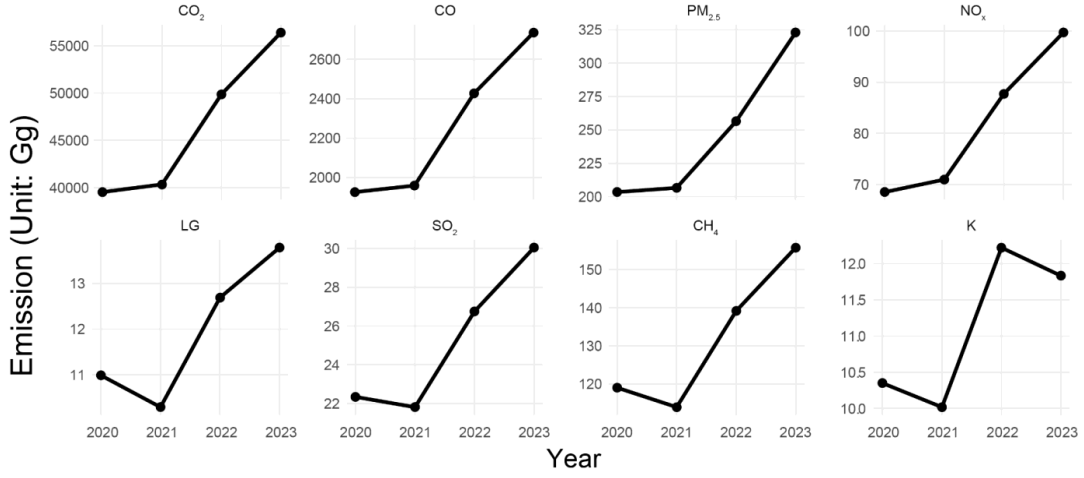

Figure 6: The trend of annual emissions for eight air pollutants from OBB in China

3.1.3 Monthly and hourly distribution

The monthly emission patterns of all eight pollutants were similar (Fig. S2), with spring (March–May) having the highest proportion of emissions, exceeding 51% of the total emissions over the four years. LG accounted for the largest proportion of total emissions during spring (up to 58%). Among the remaining three seasons, autumn (September-November) and winter (December-February) showed similar emission shares (15-17%). In contrast, summer (June-August) exhibited the lowest shares, with all eight pollutants below 15%.

While April consistently recorded the highest emissions of all eight pollutants from 2020 to 2022, the peak shifted to March in 2023. The CO_2 emissions value in March 2023 was 2.5 times higher than the average of the previous three years. At the same time, emissions in April 2023 did not decline rapidly, and the peak emission period was extended to two months. The emission from cropland fires accounted for more than 50% of the total emissions in spring, with CH_4 contributing over 75%. This indicated that the duration of cropland fires in spring had advanced and extended.

Monthly emission patterns varied by OBB type. Evergreen forest fires accounted for 44.6% of the total emissions in winter, while emissions peaked in spring for all the other OBB types. In winter, northern China faces low temperatures and snowfall, which restricts OBB activities. In contrast, the southwest's warm and dry winter climate supports forest fires. As evergreen forests were mainly found in this region, they became the primary source of wintertime pollutant emissions.

Figure S3 shows the hourly distribution of biomass burned from different types of fires and CO_2 emissions. The max emissions from cropland and grassland typically were found between 12:00 and 13:00 daily, accounting for about 46% of daily emissions

https://doi.org/10.5194/essd-2025-427
Preprint. Discussion started: 27 December 2025

from the OBB in croplands, which may be closely related to human activities. On the other hand, A smaller peak in emissions from cropland and grassland fires occurred at midnight. That is to say, the hourly emission distributions of CO_2 exhibited a bimodal characteristic. The hourly emission distributions of other pollutants were similar to those of CO_2. Additionally, fire point data from 9:00 to 11:00 and 22:00 to 0:00 the next day were only provided by geostationary satellites, which correspond to the periods of two peaks. The absence of geostationary satellite observations could preclude reliable quantification of emissions during peak activity periods.

3.2 Spatial distribution

The spatial distribution of emissions for all eight pollutants showed a high degree of consistency, owing to the similar fire locations. As an example, Figure 7 displays the annual CO_2 emissions by grid. Over the four years, the spatial distribution of pollutant emissions stayed relatively stable. Hotspots remained concentrated in Northeast and Southwest China. Low-intensity emission centers were scattered across other regions. Specifically, Northwest China had low emissions, but BA increased year by year. The number of grids with fire points increased fastest in Tibet, 15.6 times more in 2023 than in 2020, followed by Qinghai (6 times). Liaoning Province had the largest reduction, with 2023 being 70% of 2020, followed by Hainan Province (80%).

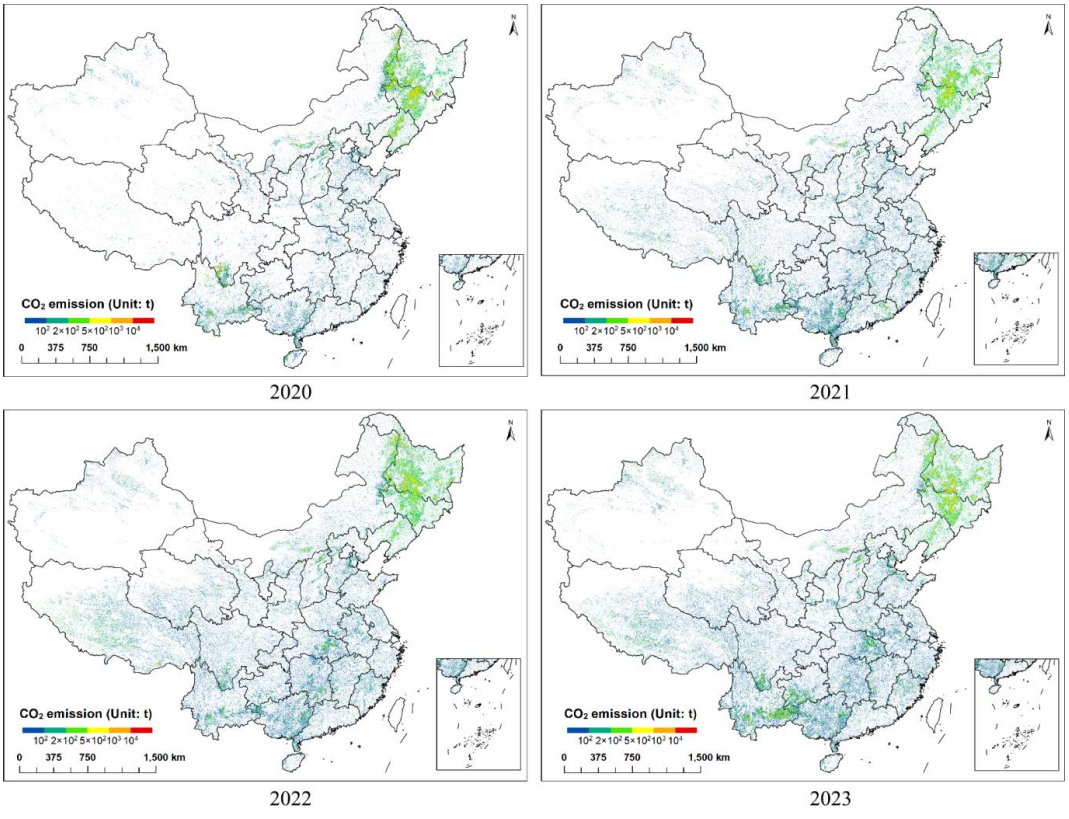

https://doi.org/10.5194/essd-2025-427
Preprint. Discussion started: 27 December 2025

Figure 7: Spatial distributions of CO_2 emissions from 2020 to 2023 in China.

Fig. 8 presents the total biomass burned from different fire types across provinces from 2020 to 2023. The spatial patterns of eight pollutant emissions were different due to fundamental differences in the geographical distribution of biomass burned from five fire types across regions and EFs.

Fig. 8(a) shows that Emissions of pollutants from evergreen forests were concentrated in the southwestern region. Among these, Yunnan Province, Sichuan Province, and the Guangxi Zhuang Autonomous Region not only had the highest total biomass burned but also ranked among the top three provinces nationwide in terms of the burning intensities (total biomass burned / the evergreen forest area in the province). In contrast, Beijing, Tianjin, and Shanghai had the lowest biomass burned. No evergreen forest fires were recorded in Tianjin and Shanghai during the study period. There were no evergreen forests in Shanghai due to the high level of urbanization. Beijing and Tianjin only had small patches of evergreen forest remaining due to the limitations of their temperate monsoon climate and the effects of urbanization. As a result, biomass burning was minimal, and the chances of fires occurring were significantly reduced.

Unlike evergreen forests, biomass burned from deciduous forests was concentrated in northeast China (Fig. 8(d)). Heilongjiang, Jilin, and the Inner Mongolia Autonomous Region were the three provinces with the highest total burned biomass, accounting for 70.6% of the national total. On the contrary, Shanghai and Guangdong had no recorded instances of deciduous forest fires. These phenomena were related to the following reasons. One was the abundant deciduous forest resources in these three northeastern provinces, accounting for 56% of the study area. The other was the climatic conditions. For example, it was drier in the northeast than in the south, which is prone to natural fires.

The cropland biomass burned was concentrated in the Northeast(Fig. 8(b)), and the amount of biomass burned in Heilongjiang(HL) province, on average, accounted for 34% of the country during the four years. However, the burning intensities on annual average were larger in southwestern provinces such as Chongqing (CQ), Guizhou (GZ), and Sichuan(SC), followed by Heilongjiang(HL) and Jilin (JL) Provinces. The burning intensity in Chongqing was the highest from 2021 to 2023, in particular. Its intensity in 2022 was 49 times higher than the lowest intensity in Gansu Province. These findings suggested that the local government should fully implement burning bans in the southwest and northeast of the country, and actively guide biomass resourcing to mitigate the environmental impact of agricultural biomass burned.

The top three largest provinces in terms of grassland biomass burned were Inner Mongolia Autonomous Region, Tibet Autonomous Region, and Sichuan Province, with the combined biomass burned in these three provinces accounting for 35.5%

https://doi.org/10.5194/essd-2025-427
Preprint. Discussion started: 27 December 2025

of the national total (Fig.8(c)). The top four lowest provinces were the four municipalities directly under the central government (Shanghai, Beijing, Tianjin, and Chongqing). Shandong Province had the highest burning intensity, possibly related to its arid climate conditions and dense human activities. Further analysis found that the biomass burned in grassland fires has increased over the four years, although the grassland area has decreased in nearly all provinces. This phenomenon contrasted with the trends observed in other fire types, indicating that grassland ecosystems may be sensitive to climate change and human disturbance. This finding underscores the challenges of grassland fire management, which must address the combined impacts of land-use changes, climate warming, and human-caused fire sources.

Other types of fires (Category Q), including those in wetlands and shrublands, contributed less to the total biomass burned. These fires were mainly concentrated in Tibet (Fig. 8(e)), which has over 6 million hectares of wetlands. Notably, biomass burned from wetlands was identified as a major contributor to the recent global increase in CH_4 concentrations (Peng et al., 2022). Therefore, wetland fires in Tibet should be paid more attention to.

On the whole, climate conditions, urbanization levels, and local management measures were key factors that influenced OBB in different provinces.

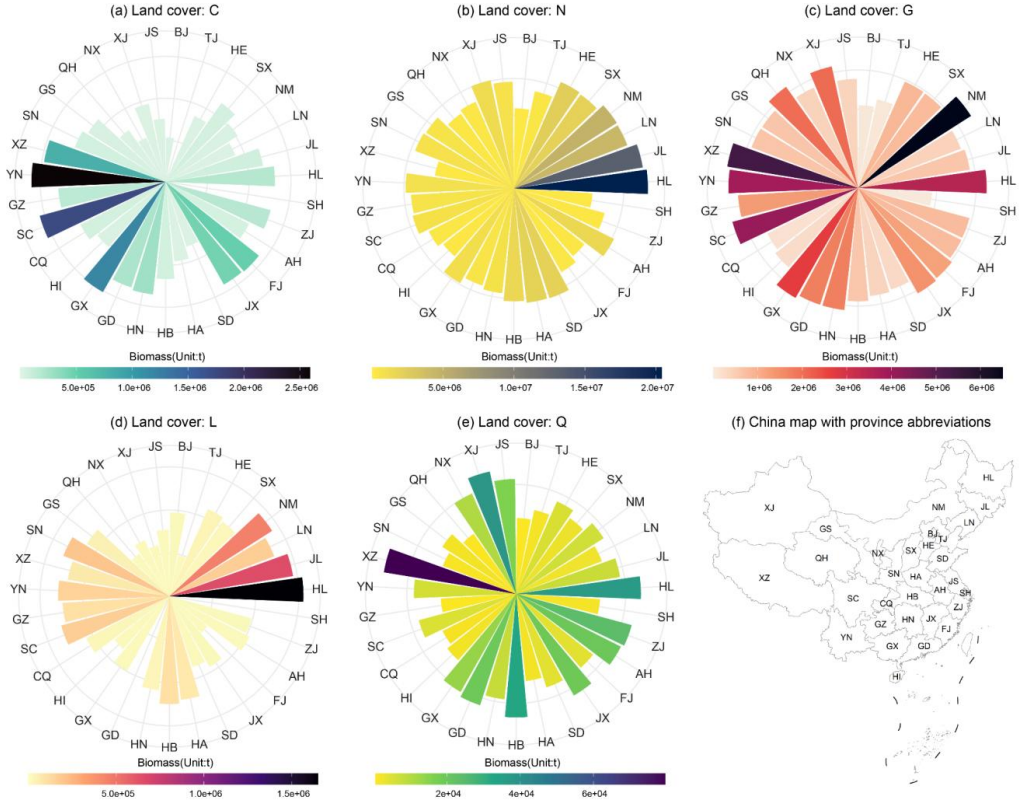

https://doi.org/10.5194/essd-2025-427
Preprint. Discussion started: 27 December 2025

Figure 8: Total biomass burned from different fire types across provinces in China from 2020 to 2023. Subplots (a-e) use a logarithmic scale in the polar coordinate system, while (f) presents an illustrative map of provincial abbreviations in China.

3.3 Method validation

3.3.1 Validation of multi-satellite data fusion

3.78 million fire points were evaluated as valid after pre-processing, and 59% of them were provided from FY-4A (7% from MODIS, and 34% from VIIRS). The number of hourly grid fire points after the spatial fusion was 2.12 million. At the same time, the proportion of fires detected by FY-4A was high in western China, particularly in Sichuan, Qinghai, and Tibet provinces (Fig.S4). The highest proportion was in Tibet, accounting for 97%. These further indicated the spatial and temporal limitations of polar orbit satellites. Therefore, the integration of multi-satellite datasets is important for accurate fire monitoring and emissions estimation.

The effectiveness of multi-satellite data fusion was evaluated using the example of a forest fire in Xichang, Sichuan Province, in 2020, as shown in Fig.9(a). Among 19 grids, there were only 4 grids (grid numbers 6,8,9,14) where all three satellites monitored the fire point at the same hour, with 3 additional grids' fire points captured only by FY-4A (grid numbers 1, 3, 17). The earliest satellite data with fire were captured by FY-4A at 8:00 AM on March 30, 2020, and the fire lasted until 00:00 on April 2, 2020, lasting about 64 hours, seven hours ahead of the official notification time. A comparison of monitoring data from different satellites for the Grid 9 is shown in Fig.9(b). The polar orbit satellites only collected data at 06:00, 15:00, and 18:00 local time. Moreover, FRP observed by the polar orbit satellites was typically slightly higher than that of FY-4A at the same time. The difference may be linked to their scanning range, time, and angle, as well as sensor type.

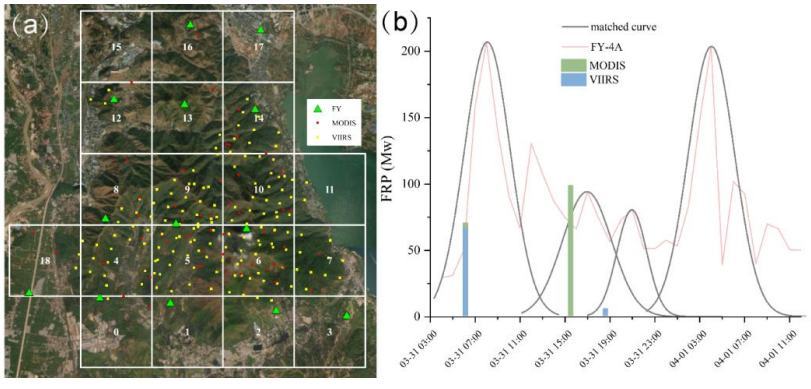

Figure 9: Satellite monitoring map of the Xichang forest fire. (a) The satellite-monitored fire point grids. The background imagery comes from World Imagery Wayback (Esri, 2022); (b) The FRP value of grid 9.

https://doi.org/10.5194/essd-2025-427
Preprint. Discussion started: 27 December 2025

3.3.2 Validation of the filtering rule

To evaluate the effectiveness of the filtering rules, we selected some of the removed fire points as examples in five grids. Satellite surface monitoring images (Esri, 2022) for these five example grids are shown in Fig.10, with the FRP of two grids also provided.

Grid 2005024 was identified as scrubland by MCD12Q1. From 2020 to 2023, this grid exhibited fire activity on approximately 260 days per year. Further investigation revealed the presence of coking companies in the grid, which could explain the prolonged heat radiation signature. Therefore, the fire point data for this grid was deleted according to Rule 1. Based on the fire frequency thresholds, we excluded 89 thousand fire points (37% of total removals), and the grids where the fire points were removed accounted for 0.1% of the total number of grids.

The land cover type of grid 34194 was cropland. The number of fires was 473 in this grid during four years, and their FRP values were below 3.5 MW. These low radiation power fires were measured only by polar orbit satellites, indicating that the fires were relatively small. Meanwhile, the fires consistently occurred between 18:00 and 20:00 each day, showing no significant seasonal variation. Furthermore, it was the cooking time in this region. It could be concluded that the fire point was generated by the residents' outdoor fire cooking. Following Rule 2, these fire point data were deleted. Rule 2 considered the threshold of radiation power of the OBB fires. Seventy-three thousand fire points were removed, accounting for 30% of the total removed fire points.

Grid 2104884 was located in Hebei province, and the fire within the grid occurred at 11:00 in January, November, and December from 2021 to 2023. All the 81 fire point information was provided by FY-4A. The regularity of the fire timing during the winter months indicated that this fire may be related to winter heating. The local heating season in Hebei begins in November and lasts until March of the following year. Meanwhile, a power company within the grid was responsible for centralized heating. Rule 3 considered the regularity of the timing of fires. 38 thousand fires, or 16% of the total number, were removed.

Grid 70910 was located in the evergreen forest area of Yunnan Province. The fire was monitored by FY-4A on February 19, 2022, and its duration was six hours. The FRP increased from 3.45 MW to 7.61 MW, finally decreasing to 6.47 MW. The standard deviation was only 1.6. Therefore, the fire point data for this grid were deleted according to rule 4. This Rule deleted 24 thousand fire points, which accounted for 10 percent of the total deleted points.

https://doi.org/10.5194/essd-2025-427
Preprint. Discussion started: 27 December 2025

Grid 52532 was situated at the intersection of towns and mountain ranges. FY-4A detected a fire point with an FRP of 173 MW on November 18, 2022, at 02:00 a.m. The previous observation, recorded at 20:00 on November 17, showed an FRP of 13 MW, while the subsequent observation at 04:00 on November 18 recorded an FRP of 10 MW. This area experienced sudden extreme values. As a result, the fire point records for this grid were deleted. Sensors have the potential for sudden monitoring errors due to refraction from clouds, bodies of water, etc (Kang et al., 2022). Rule 5 considered the unnaturalness of such extreme fluctuations and deleted 18 thousand fire points, which accounted for 8% of the total number of removed fire points.

In summary, these five rules we developed effectively removed 243 thousand fire points. Finally, we had a total of 1.88 million hourly fire points in grids. Compared to the fire points after spatial fusion during the four years, the removed fire points accounted for 11%. The removed fire points were concentrated in approximately 5,000 suspicious grids, which were distributed in all provinces of China and usually localized in the WUI. These five rules minimized data bias, removed outliers, and reduced the uncertainty of activity levels in the datasets.

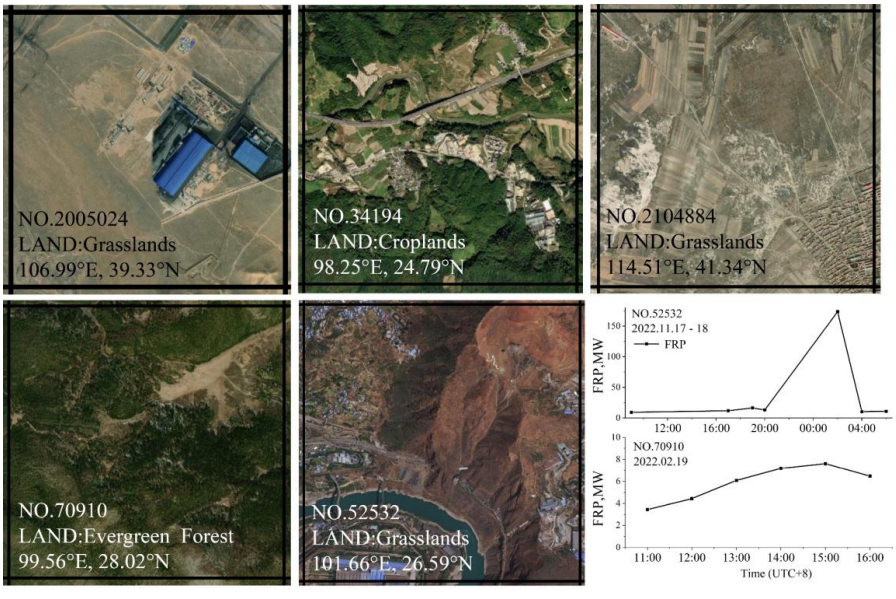

Figure 10: Satellite surface monitoring map of suspicious grids and FRP variations. The "LAND" for each grid represents the land cover type determined by the MCD12Q1 dataset. The background imagery comes from World Imagery Wayback (Esri, 2022).

3.4 Uncertainty

The COBBEI still had some uncertainty. The sources of this uncertainty included satellite monitoring capabilities, the accuracy of land cover maps, EFs, and so on (Liu et al., 2020). First, there were systematic deviations due to different satellites and their resolutions(Hua et al., 2024). Although the FY-4A, as China's first geostationary satellite with a radiation imager, bridges the monitoring gaps in western China left by the other geostationary satellites, its FHS product was less accurate compared to

https://doi.org/10.5194/essd-2025-427
Preprint. Discussion started: 27 December 2025

other advanced radiation imagers (Celiz et al., 2021). The low spatial resolution of geostationary satellites may leave SFs' data missing. On the other hand, the two types of polar orbit satellites may miss fires outside their monitoring time.

Second, the accuracy of the land cover maps was about 75% (Friedl et al., 2010). The accuracy of MCD12Q1 declined in the ecologically vulnerable South China Karst, where terrain variability was high. In regions with altitudes above 1,200 m or slopes greater than 25°, the accuracy reached 41% (Liu et al., 2022). While the filtering rules based on FRP characteristics may reduce uncertainty from land cover misclassification, some degree of omission and misclassification remained. At the same time, the hierarchical classification system of land cover maps affects fuel loading and the fraction of biomass burned, contributing to biases in emissions. The categorization in the MCD12Q1 product (e.g., cropland) lacks finer sub-categorization, which could also create uncertainty in emissions.

Third, EFs directly affected the emissions. However, the EFs for the same land cover type span a broad range according to the literature. The most extensive range of EFs for the same land cover type in Table S3 was CH_4 EFs in croplands, with the maximum value (9.59, (Christian et al., 2003)) being 3.4 times higher than the minimum value (2.79, (Stockwell et al., 2016)), the two sets of data were obtained from laboratory measurements of biomass burned in Indonesia and field measurements of crop residue in Nepal, respectively. Therefore, the median EF values from recent literature were selected to calculate emissions in this study. Meanwhile, we reclassified the 16 land use types into five broad categories to simplify the calculations, further expanding the range of EFs. Although we used the median to minimize the influence of extreme values, some differences remain compared to actual and local EFs.

Fourth, the biomass burned was calculated by integrating the FRP cycle. This method allowed us to convert scattered data into a curve. Uncertainties in the fitted parameters could propagate to the final emissions. For example, the R^2 of BD and FRP ranges from 0.53 to 0.98. The lower the R^2, the higher the coefficient of variation and the higher the uncertainty. Thus, the uncertainty of BD in Region D of the cropland was the highest among all the subareas.

3.5 Comparison with other studies

A few studies have estimated pollutants emitted from OBB in China using satellite data. The CO_2 emission in 2020 was chosen to compare with others, as shown in Table 2. The CHOBE data were directly from the literature, and the rest were calculated using the datasets according to the literature method. Among all datasets, COBBEI reported the lowest values, with the main differences stemming from the reconstruction of FRP cycles based on land cover, the selected EFs, and the applied filtering rules.

https://doi.org/10.5194/essd-2025-427
Preprint. Discussion started: 27 December 2025

The fitted curve integrals were directly related to the biomass burned. Compared to other datasets that use the FRP curve integral approach, the average COBBEI fitted curve integral was only 37% of that of CHOBE (Xu et al., 2023). This leads to differences in the translation from FRP to biomass, further affecting the results. The FRP curve in this study fitted well with the BD of the fire, better representing the biomass burned.

The EF value also played a critical role in the emission inventories. CHOBE used regression models to estimate EFs, resulting in a CO_2 EF for cropland that was 1.5 times higher than that used in COBBEI. GFEDv5 (Wiggins et al., 2021) derived forest EFs through in situ measurements, which focused on fires with well-developed plumes during the daytime. This incomplete sampling method resulted in the forest CO_2 EF used by GFEDv5 being 1.06 times that used by COBBEI.

Notably, the application of our filtering rules eliminated 243 thousand fire points, substantially impacting the results. These rules resulted in a 10% reduction in CO_2 emissions. Other studies typically used only land cover maps to determine whether fires were from OBB.

Overall, the CO_2 emissions in 2020 from the literature were about 1.1-7.8 times higher than in COBBEI. The supplement material compared GFEDv4.1, GFEDv5, and COBBEI regarding yearly changes and spatial distribution of the different pollutants. GFEDv5 reported significantly higher emissions than both GFEDv4.1 and COBBEI, except for CH_4. Notably, GFEDv5 exhibited a marked decline across all pollutants in 2021. Regarding spatial patterns, COBBEI displayed more regional variability than the two GFED datasets. Differences in satellite data fusion, EFs, and corrections for small and unclear fires among various datasets may result in significant gaps in the spatial and temporal distribution of OBB emission datasets (Carter et al., 2020; Hua et al., 2024; Schollaert et al., 2024; Synolakis and Karagiannis, 2024).

Table 2: Comparison of estimation methods for different datasets and OBB CO_2 emissions in 2020.

Datasets	Sources	Satellites	Methods	Annual emission (Mt)
COBBEI	This study	G+P(3)	FRP	39
CHOBE	(Xu et al., 2023)	G+P(3)	FRP	306
GFEDv4.1	(van der Werf et al., 2017)	P(2)	BA	42
FINNv1.5	(Wiedinmyer et al., 2011)	P(2)	BA	53
GFEDv5	(Chen et al., 2023)	P(3)	BA	97

Note. In the 'Satellites' column, G represents geostationary satellites, and P represents polar orbit satellites. The numbers in parentheses indicate the total number of radiation images used.

https://doi.org/10.5194/essd-2025-427
Preprint. Discussion started: 27 December 2025

4. Data availability

The COBBEI dataset can be downloaded at https://figshare.com (last access: 2025-06-20) with the following DOI: https://doi.org/10.6084/m9.figshare.29367869.v1(Shi and Ji, 2025).

5. Conclusions

In this study, a high-resolution emission inventory of OBB in China for 2020-2023, named COBBEI, was constructed. The dataset included eight pollutants: CO_2, CO, CH_4, NO_X, SO_2, $PM_{2.5}$, K, and LG, with a temporal resolution of 1 hour and a spatial resolution of 2 km. This was the first time to fuse FRP data from the FY-4A geostationary satellite and polar orbit satellites. This study considered five types of OBB fires in China and reconstructed the FRP curves from the fused data. This study identified 2.12 million valid hourly fire points. The FY-4A satellite provided 59% of the fire point data. Five filtering rules have been proposed and proven to be effective. Fifty nine optimal fit equations for FRP versus BD were constructed using the Gaussian function. The function parameters were determined using k-median. We also collected EFs from the literature and used the median value of all data for EFs in COBBEI.

From 2020 to 2023, the annual average emissions of CO_2, CO, CH_4, NO_x, SO_2, $PM_{2.5}$, K, and LG were 46530, 2262, 132, 82, 25, 247, 11, and 12 Gg, respectively. During four years, eight pollutants exhibited three distinct interannual patterns. The total annual CO_2, CO, NO_x, and $PM_{2.5}$ emissions increased yearly. In contrast, CH_4, SO_2, and LG emissions followed a V-shaped trend, slightly declining in 2021. The annual emissions of K fluctuated throughout four years. The monthly emission patterns for all eight pollutants were similar. Spring consistently had the highest share of emissions, with all eight pollutants contributing more than 51% of the total emissions over the four years. Fires in cropland and grassland typically reached emission peaks between 11:00 and 13:00 daily.

In summary, the spatial distribution of all eight pollutant emissions over the four years remained relatively stable, with persistent hotspots concentrated in Northeast and Southwest China and scattered low-intensity emission centers in other regions. However, spatial patterns of biomass burned from different fire types revealed distinct regional characteristics: evergreen forest fires were prevalent in the southwest. In contrast, deciduous forest fires were distributed mainly in the northeast. Grassland fires were concentrated in Inner Mongolia, and cropland fires were most common in the northeastern provinces. Other fire types, such as wetland and shrubland fires, were mainly observed in Tibet.

The COBBEI may provide crucial data for numerical air quality models, environmental policy-making, and fire emergency responses. There are three key directions for future research. First, improving the collaboration between satellite remote

https://doi.org/10.5194/essd-2025-427
Preprint. Discussion started: 27 December 2025

sensing and ground observations will help enhance monitoring accuracy through multi-satellite data fusion. Second, developing differentiated calculation methods for fires of different sizes will improve the accuracy of emission estimates. Third, advancing the measurement of localized EFs in China is crucial.

Author contributions

JWS and YQJ developed the algorithm and created and validated the dataset. JWS and WJX conceived the paper. JWS, YXZ, XCZ, and YSM conducted the data processing. JWS, RXS, and JFM analyzed the data and produced figures. YQJ, JWS, and YCF reviewed and revised the paper.

Competing interests.

The contact author has declared that none of the authors has any competing interests.

Acknowledgements.

During the preparation of this work, the authors used ChatGPT in order to improve the language. After using this tool, the authors reviewed and edited the content as needed and take full responsibility for the content of the publication.

References

Aguilera, R., Corringham, T., Gershunov, A., and Benmarhnia, T.: Wildfire smoke impacts respiratory health more than fine particles from other sources: Observational evidence from Southern California, Nat Commun, 12, 1493, https://doi.org/10.1038/s41467-021-21708-0, 2021.

Andela, N., Morton, D. C., Giglio, L., Paugam, R., Chen, Y., and Hantson, S.: The Global Fire Atlas of individual fire size, duration, speed and direction, Earth System Science Data, 529–552, https://doi.org/10.5194/essd-11-529-2019, 2019.

Burke, M., Driscoll, A., Heft-Neal, S., Xue, J., Burney, J., and Wara, M.: The changing risk and burden of wildfire in the United States, PNAS, 118, e2011048118, https://doi.org/10.1073/pnas.2011048118, 2020.

Carter, T. S., Heald, C. L., Jimenez, J. L., Campuzano-Jost, P., Kondo, Y., Moteki, N., Schwarz, J. P., Wiedinmyer, C., Darmenov, A. S., da Silva, A. M., and Kaiser, J. W.: How emissions uncertainty influences the distribution and radiative impacts of smoke from fires in North America, Atmospheric Chemistry and Physics, 20, 2073–2097, https://doi.org/10.5194/acp-20-2073-2020, 2020.

https://doi.org/10.5194/essd-2025-427
Preprint. Discussion started: 27 December 2025

Casey, J. A., Kioumourtzoglou, A., Padula, A., González, D. J. X., Elser, H., Aguilera, R., Northrop, A. J., Tartof, S. Y., Mayeda, E. R., Braun, D., Dominici, F., Eisen, E. A., Morello, R., and Benmarhnia, T.: Measuring long-term exposure to wildfire $PM_{2.5}$ in California: Time-varying inequities in environmental burden, PNAS, 121, https://doi.org/10.1073/pnas.2306729121, 2024.

Celiz, M. A. D. A., Landero, R. R., Principe, J. A., and Ang, M. R. C. O.: Accuracy assessment of FY-4A fire/hotspot(FHS) product in wildfire detection, Int. Arch. Photogramm. Remote Sens. Spatial Inf. Sci., XLVI-4/W6-2021, 91–96, https://doi.org/10.5194/isprs-archives-XLVI-4-W6-2021-91-2021, 2021.

Chen, Y., Hall, J., Van Wees, D., Andela, N., Hantson, S., Giglio, L., Van Der Werf, G. R., Morton, D. C., and Randerson, J. T.: Multi-decadal trends and variability in burned area from the fifth version of the Global Fire Emissions Database (GFED5), Earth Syst. Sci. Data, 15, 5227–5259, https://doi.org/10.5194/essd-15-5227-2023, 2023.

Cheng, Z., Wang, S., Fu, X., Watson, J. G., Jiang, J., Fu, Q., Chen, C., Xu, B., Yu, J., Chow, J. C., and Hao, J.: Impact of biomass burning on haze pollution in the Yangtze River delta, China: A case study in summer 2011, Atmospheric Chemistry and Physics, 14, 4573–4585, https://doi.org/10.5194/acp-14-4573-2014, 2014.

China Meteorological Administration: China Climate Bulletin (2022), China Meteorological Administration, 2023.

Christian, T. J., Kleiss, B., Yokelson, R. J., Holzinger, R., Crutzen, P. J., Hao, W. M., Saharjo, B. H., and Ward, D. E.: Comprehensive laboratory measurements of biomass-burning emissions: 1. Emissions from Indonesian, African, and other fuels, Journal of Geophysical Research: Atmospheres, 108, https://doi.org/10.1029/2003JD003704, 2003.

Esri: World Imagery Wayback, China, 2022.

Ferrada, G. A., Zhou, M., Wang, J., Lyapustin, A., Wang, Y., Freitas, S. R., and Carmichael, G. R.: Introducing the VIIRS-based fire emission inventory version 0 (VFEIv0), Geoscientific Model Development, 15, 8085–8109, https://doi.org/10.5194/gmd-15-8085-2022, 2022.

Freeborn, P. H., Wooster, M. J., Roy, D. P., and Cochrane, M. A.: Quantification of MODIS fire radiative power (FRP) measurement uncertainty for use in satellite-based active fire characterization and biomass burning estimation, Geophys. Res. Lett., 41, 1988–1994, https://doi.org/10.1002/2013GL059086, 2014.

Friedl, M. and Sulla-Menashe, D.: MODIS/Terra+Aqua Land Cover Type Yearly L3 Global 500m SIN Grid V061, https://doi.org/10.5067/MODIS/MCD12Q1.061, 2022.

https://doi.org/10.5194/essd-2025-427
Preprint. Discussion started: 27 December 2025

Friedl, M. A., Sulla-Menashe, D., Tan, B., Schneider, A., Ramankutty, N., Sibley, A., and Huang, X.: MODIS Collection 5 global land cover: Algorithm refinements and characterization of new datasets, Remote Sensing of Environment, 114, 168–182, https://doi.org/10.1016/j.rse.2009.08.016, 2010.

Ghetu, C. C., Rohlman, D., Smith, B. W., Scott, R. P., Adams, K. A., Hoffman, P. D., and Anderson, K. A.: Wildfire impact on indoor and outdoor PAH air quality, Environ. Sci. Technol., 10042–10052, https://doi.org/10.1021/acs.est.2c00619, 2022.

Holden, Z. A., Swanson, A., Luce, C. H., Jolly, W. M., Maneta, M., Oyler, J. W., Warren, D. A., Parsons, R., and Affleck, D.: Decreasing fire season precipitation increased recent western US forest wildfire activity, Proc. Natl. Acad. Sci. U.S.A., 115, https://doi.org/10.1073/pnas.1802316115, 2018.

Hua, W., Lou, S., Huang, X., Xue, L., Ding, K., Wang, Z., and Ding, A.: Diagnosing uncertainties in global biomass burning emission inventories and their impact on modeled air pollutants, Atmos. Chem. Phys., 24, 6787–6807, https://doi.org/10.5194/acp-24-6787-2024, 2024.

Jiang, K., Xing, R., Luo, Z., Huang, W., Yi, F., Men, Y., Zhao, N., Chang, Z., Zhao, J., Pan, B., and Shen, G.: Pollutant emissions from biomass burning: A review on emission characteristics, environmental impacts, and research perspectives, Particuology, 85, 296–309, https://doi.org/10.1016/j.partic.2023.07.012, 2024.

Jones, M. W., Abatzoglou, J. T., Veraverbeke, S., Andela, N., Lasslop, G., Forkel, M., Smith, A. J. P., Burton, C., Betts, R. A., Van Der Werf, G. R., Sitch, S., Canadell, J. G., Santín, C., Kolden, C., Doerr, S. H., and Le Quéré, C.: Global and regional trends and drivers of fire under climate change, Reviews of Geophysics, 60, e2020RG000726, https://doi.org/10.1029/2020RG000726, 2022.

Kang, Y., Jang, E., Im, J., and Kwon, C.: A deep learning model using geostationary satellite data for forest fire detection with reduced detection latency, GIScience & Remote Sensing, 59, 2019–2035, https://doi.org/10.1080/15481603.2022.2143872, 2022.

Ke, H., Gong, S., He, J., Zhou, C., Zhang, L., and Zhou, Y.: Spatial and temporal distribution of open bio-mass burning in China from 2013 to 2017, Atmospheric Environment, 210, 156–165, https://doi.org/10.1016/j.atmosenv.2019.04.039, 2019.

Khan, J. Z., Sun, L., Tian, Y., Shi, G., and Feng, Y.: Chemical characterization and source apportionment of PM_1 and $PM_{2.5}$ in Tianjin, China: Impacts of biomass burning and primary biogenic sources, Journal of Environmental Sciences, 99, 196–209, https://doi.org/10.1016/j.jes.2020.06.027, 2021.

https://doi.org/10.5194/essd-2025-427
Preprint. Discussion started: 27 December 2025

Korsiak, J., Pinault, L., Christidis, T., Burnett, R. T., Abrahamowicz, M., and Weichenthal, S.: Long-term exposure to wildfires and cancer incidence in Canada: A population-based observational cohort study, The Lancet Planetary Health, 6, e400–e409, https://doi.org/10.1016/S2542-5196(22)00067-5, 2022.

LANCEMODIS: MODIS/Aqua Terra Thermal Anomalies/Fire locations 1km FIRMS NRT (Vector data), https://doi.org/10.5067/FIRMS/MODIS/MCD14DL.NRT.0061, 2021.

Li, F., Zhang, X., Roy, D. P., and Kondragunta, S.: Estimation of biomass-burning emissions by fusing the fire radiative power retrievals from polar-orbiting and geostationary satellites across the conterminous United States, Atmospheric Environment, 211, 274–287, https://doi.org/10.1016/j.atmosenv.2019.05.017, 2019.

Li, F., Zhang, X., Kondragunta, S., Lu, X., Csiszar, I., and Schmidt, C. C.: Hourly biomass burning emissions product from blended geostationary and polar-orbiting satellites for air quality forecasting applications, Remote Sensing of Environment, 281, 113237, https://doi.org/10.1016/j.rse.2022.113237, 2022.

Li S., Zhang Y., and Zhang X.: Measurement and spatio-temporal evolution of straw utilization efficiency in china, Journal of Central South University of Forestry & Technology (Social Sciences）, 18, 43–57, https://doi.org/10.14067/j.cnki.1673-9272.2024.05.005, 2024.

Liu, M., Song, Y., Yao, H., Kang, Y., Li, M., Huang, X., and Hu, M.: Estimating emissions from agricultural fires in the North China Plain based on MODIS fire radiative power, Atmospheric Environment, 112, 326–334, https://doi.org/10.1016/j.atmosenv.2015.04.058, 2015.

Liu, P., Pei, J., Guo, H., Tian, H., Fang, H., and Wang, L.: Evaluating the accuracy and spatial agreement of five global land cover satasets in the ecologically vulnerable South China Karst, Remote Sensing, 14, 3090, https://doi.org/10.3390/rs14133090, 2022.

Liu, T., Mickley, L. J., Marlier, M. E., DeFries, R. S., Khan, M. F., Latif, M. T., and Karambelas, A.: Diagnosing spatial biases and uncertainties in global fire emissions inventories: Indonesia as regional case study, Remote Sensing of Environment, 237, 111557, https://doi.org/10.1016/j.rse.2019.111557, 2020.

Liu, Y., Chen, J., Shi, Y., Zheng, W., Shan, T., and Wang, G.: Global Emissions Inventory from Open Biomass Burning (GEIOBB): utilizing Fengyun-3D global fire spot monitoring data, Earth System Science Data, 16, 3495–3515, https://doi.org/10.5194/essd-16-3495-2024, 2024.

https://doi.org/10.5194/essd-2025-427
Preprint. Discussion started: 27 December 2025

615 Molitor, D., Mullins, J. T., and White, C.: Air pollution and suicide in rural and urban America: Evidence from wildfire smoke, Proc. Natl. Acad. Sci. U.S.A., 120, e2221621120, https://doi.org/10.1073/pnas.2221621120, 2023.

Mota, B. and Wooster, M. J.: A new top-down approach for directly estimating biomass burning emissions and fuel consumption rates and totals from geostationary satellite fire radiative power (FRP), Remote Sensing of Environment, 206, 45–62, https://doi.org/10.1016/j.rse.2017.12.016, 2018.

620 NASA VIIRS Land Science Team: VIIRS (NOAA-20/JPSS-1) I Band 375 m Active Fire Product NRT (Vector data), https://doi.org/10.5067/FIRMS/VIIRS/VJ114IMGT_NRT.002%20Date, 2020.

National Satellite Meteorological Center: FY-4A AGRI L2 Fire/Hot spot detection product, 2024.

Ning, X., Li, J., Zhuang, P., Lai, S., and Zheng, X.: Wildfire combustion emission inventory in Southwest China (2001-2020) based on MODIS fire radiative energy data, Atmospheric Pollution Research, 15, 102279,
625 https://doi.org/10.1016/j.apr.2024.102279, 2024.

Peng, S., Lin, X., Thompson, R. L., Xi, Y., Liu, G., Hauglustaine, D., Lan, X., Poulter, B., Ramonet, M., Saunois, M., Yin, Y., Zhang, Z., Zheng, B., and Ciais, P.: Wetland emission and atmospheric sink changes explain methane growth in 2020, Nature, 612, 477–482, https://doi.org/10.1038/s41586-022-05447-w, 2022.

Piedrahita, V. A., Roberts, A. P., Rohling, E. J., Heslop, D., Zhao, X., Galeotti, S., Florindo, F., Grant, K. M., Hu, P., and Li,
630 J.: Dry hydroclimates in the late Palaeocene-early Eocene hothouse world, Nat Commun, 15, 7042, https://doi.org/10.1038/s41467-024-51430-6, 2024.

Qiu, X., Duan, L., Chai, F., Wang, S., Yu, Q., and Wang, S.: Deriving High-Resolution Emission Inventory of Open Biomass Burning in China based on Satellite Observations, Environ. Sci. Technol., 50, 11779–11786, https://doi.org/10.1021/acs.est.6b02705, 2016.

635 Ravindra, K., Sokhi, R., and Vangrieken, R.: Atmospheric polycyclic aromatic hydrocarbons: Source attribution, emission factors and regulation, Atmospheric Environment, 42, 2895–2921, https://doi.org/10.1016/j.atmosenv.2007.12.010, 2008.

Reid, J. S., Hyer, E. J., Prins, E. M., Westphal, D. L., Zhang, J., Wang, J., Christopher, S. A., Curtis, C. A., Schmidt, C. C., Eleuterio, D. P., Richardson, K. A., and Hoffman, J. P.: Global monitoring and forecasting of biomass-burning smoke: Description of and lessons from the fire locating and modeling of burning emissions (FLAMBE) program, IEEE Journal of
640 Selected Topics in Applied Earth Observations and Remote Sensing, 2, 144–162, https://doi.org/10.1109/JSTARS.2009.2027443, 2009.

https://doi.org/10.5194/essd-2025-427
Preprint. Discussion started: 27 December 2025

Schollaert, C. L., Marlier, M. E., and Busch Isaksen, T. M.: Development of a source-specific biomass burning emissions inventory for Washington, Oregon, and California, Atmospheric Environment, 319, 120283, https://doi.org/10.1016/j.atmosenv.2023.120283, 2024.

Shabbir, A. H., Ji, J., Groninger, J. W., Gueye, G. N., Knouft, J. H., van Etten, E. J. B., and Zhang, J.: Climate predicts wildland fire extent across China, Science of The Total Environment, 896, 164987, https://doi.org/10.1016/j.scitotenv.2023.164987, 2023.

Shi, J. and Ji, Y.: COBBEI: China Open Biomass Burning Emission Inventory, https://doi.org/10.6084/m9.figshare.29367869.v1, 2025.

Simões Amaral, S., Andrade De Carvalho, J., Martins Costa, M., and Pinheiro, C.: Particulate matter emission factors for biomass combustion, Atmosphere, 7, 141, https://doi.org/10.3390/atmos7110141, 2016.

Stockwell, C. E., Christian, T. J., Goetz, J. D., Jayarathne, T., Bhave, P. V., Praveen, P. S., Adhikari, S., Maharjan, R., DeCarlo, P. F., Stone, E. A., Saikawa, E., Blake, D. R., Simpson, I. J., Yokelson, R. J., and Panday, A. K.: Nepal Ambient Monitoring and Source Testing Experiment (NAMaSTE): Emissions of trace gases and light-absorbing carbon from wood and dung cooking fires, garbage and crop residue burning, brick kilns, and other sources, Atmospheric Chemistry and Physics, 16, 11043–11081, https://doi.org/10.5194/acp-16-11043-2016, 2016.

Synolakis, C. E. and Karagiannis, G. M.: Wildfire risk management in the era of climate change, PNAS Nexus, 3, 151, https://doi.org/10.1093/pnasnexus/pgae151, 2024.

Urbanski, S. P., Hao, W. M., and Baker, S.: Chapter 4 Chemical composition of wildland fire emissions, in: Developments in Environmental Science, vol. 8, edited by: Bytnerowicz, A., Arbaugh, M. J., Riebau, A. R., and Andersen, C., Elsevier, 79–107, https://doi.org/10.1016/S1474-8177(08)00004-1, 2008.

Vermote, E., Ellicott, E., Dubovik, O., Lapyonok, T., Chin, M., Giglio, L., and Roberts, G. J.: An approach to estimate global biomass burning emissions of organic and black carbon from MODIS fire radiative power, Journal of Geophysical Research: Atmospheres, 114, https://doi.org/10.1029/2008JD011188, 2009.

van der Werf, G. R., Randerson, J. T., Giglio, L., van Leeuwen, T. T., Chen, Y., Rogers, B. M., Mu, M., van Marle, M. J. E., Morton, D. C., Collatz, G. J., Yokelson, R. J., and Kasibhatla, P. S.: Global fire emissions estimates during 1997-2016, Earth System Science Data, 9, 697–720, https://doi.org/10.5194/essd-9-697-2017, 2017.

https://doi.org/10.5194/essd-2025-427
Preprint. Discussion started: 27 December 2025

Wiedinmyer, C., Akagi, S. K., Yokelson, R. J., Emmons, L. K., Al-Saadi, J. A., Orlando, J. J., and Soja, A. J.: The Fire Inventory from NCAR (FINN): A high resolution global model to estimate the emissions from open burning, Geosci. Model Dev., 4, 625–641, https://doi.org/10.5194/gmd-4-625-2011, 2011.

Wiedinmyer, C., Kimura, Y., McDonald-Buller, E. C., Emmons, L. K., Buchholz, R. R., Tang, W., Seto, K., Joseph, M. B., Barsanti, K. C., Carlton, A. G., and Yokelson, R.: The Fire inventory from NCAR version 2.5: An updated global fire emissions model for climate and chemistry applications, Geoscientific Model Development, 16, 3873–3891, https://doi.org/10.5194/gmd-16-3873-2023, 2023.

Wiggins, E. B., Anderson, B. E., Brown, M. D., Campuzano-Jost, P., Chen, G., Crawford, J., Crosbie, E. C., Dibb, J., DiGangi, J. P., Diskin, G. S., Fenn, M., Gallo, F., Gargulinski, E. M., Guo, H., Hair, J. W., Halliday, H. S., Ichoku, C., Jimenez, J. L., Jordan, C. E., Katich, J. M., Nowak, J. B., Perring, A. E., Robinson, C. E., Sanchez, K. J., Schueneman, M., Schwarz, J. P., Shingler, T. J., Shook, M. A., Soja, A. J., Stockwell, C. E., Thornhill, K. L., Travis, K. R., Warneke, C., Winstead, E. L., Ziemba, L. D., and Moore, R. H.: Reconciling assumptions in bottom-up and top-down approaches for estimating aerosol emission rates from wildland fires using observations from FIREX-AQ, Journal of Geophysical Research: Atmospheres, 126, e2021JD035692, https://doi.org/10.1029/2021JD035692, 2021.

Wooster, M. J., Roberts, G., Perry, G. L. W., and Kaufman, Y. J.: Retrieval of biomass combustion rates and totals from fire radiative power observations: FRP derivation and calibration relationships between biomass consumption and fire radiative energy release, Journal of Geophysical Research: Atmospheres, 110, https://doi.org/10.1029/2005JD006318, 2005.

Wooster, M. J., Roberts, G. J., Giglio, L., Roy, D. P., Freeborn, P. H., Boschetti, L., Justice, C., Ichoku, C., Schroeder, W., Davies, D., Smith, A. M. S., Setzer, A., Csiszar, I., Strydom, T., Frost, P., Zhang, T., Xu, W., de Jong, M. C., Johnston, J. M., Ellison, L., Vadrevu, K., Sparks, A. M., Nguyen, H., McCarty, J., Tanpipat, V., Schmidt, C., and San-Miguel-Ayanz, J.: Satellite remote sensing of active fires: History and current status, applications and future requirements, Remote Sensing of Environment, 267, 112694, https://doi.org/10.1016/j.rse.2021.112694, 2021.

Wu, J., Kong, S., Zeng, X., Cheng, Y., Yan, Q., Zheng, H., Yan, Y., Zheng, S., Liu, D., Zhang, X., Fu, P., Wang, S., and Qi, S.: First high-resolution emission inventory of levoglucosan for biomass burning and non-biomass burning sources in China, Environ. Sci. Technol., 55, 1497–1507, https://doi.org/10.1021/acs.est.0c06675, 2021.

Xu, W.: Improvements in high-temporal resolution active fire detection and FRP retrieval over the Americas using GOES-16 ABI with the geostationary Fire Thermal Anomaly (FTA) algorithm, Science of Remote Sensing, 100016, https://doi.org/10.1016/j.srs.2021.100016, 2021.

https://doi.org/10.5194/essd-2025-427
Preprint. Discussion started: 27 December 2025

Xu, Y., Huang, Z., Ou, J., Jia, G., Wu, L., Liu, H., Lu, M., Fan, M., Wei, J., Chen, L., and Zheng, J.: Near-real-time estimation of hourly open biomass burning emissions in China using multiple satellite retrievals, Science of The Total Environment, 817, 152777, https://doi.org/10.1016/j.scitotenv.2021.152777, 2022.

Xu, Y., Huang, Z., Ye, J., and Zheng, J.: Hourly emissions of air pollutants and greenhouse gases from open biomass burning in China during 2016–2020, Sci Data, 10, 629, https://doi.org/10.1038/s41597-023-02541-0, 2023.

Xue, T., Geng, G., Han, Y., Wang, H., Li, J., Li, H., Zhou, Y., and Zhu, T.: Open fire exposure increases the risk of pregnancy loss in South Asia, Nat Commun, 12, 3205, https://doi.org/10.1038/s41467-021-23529-7, 2021.

Xue, T., Li, J., Tong, M., Fan, X., Li, P., Wang, R., Li, Y., Zheng, Y., Li, J., Guan, T., and Zhu, T.: Stillbirths attributable to open fires and their geographic disparities in non-Western countries, Environmental Pollution, 334, 122170, https://doi.org/10.1016/j.envpol.2023.122170, 2023.

Yang, G., Zhao, H., Tong, D. Q., Xiu, A., Zhang, X., and Gao, C.: Impacts of post-harvest open biomass burning and burning ban policy on severe haze in the Northeastern China, Science of The Total Environment, 716, 136517, https://doi.org/10.1016/j.scitotenv.2020.136517, 2020.

Yang, Y. and Zhao, Y.: Quantification and evaluation of atmospheric pollutant emissions from open biomass burning with multiple methods: a case study for the Yangtze River Delta region, China, Atmospheric Chemistry and Physics, 19, 327–348, https://doi.org/10.5194/acp-19-327-2019, 2019.

Ye, T., Xu, R., Yue, X., Chen, G., Yu, P., Coêlho, M. S. Z. S., Saldiva, P. H. N., Abramson, M. J., Guo, Y., and Li, S.: Short-term exposure to wildfire-related $PM_{2.5}$ increases mortality risks and burdens in Brazil, Nat Commun, 13, 7651, https://doi.org/10.1038/s41467-022-35326-x, 2022.

Ye, X., Arab, P., Ahmadov, R., James, E., Grell, G. A., Pierce, B., Kumar, A., Makar, P., Chen, J., Davignon, D., Carmichael, G. R., Ferrada, G., McQueen, J., Huang, J., Kumar, R., Emmons, L., Herron-Thorpe, F. L., Parrington, M., Engelen, R., Peuch, V.-H., da Silva, A., Soja, A., Gargulinski, E., Wiggins, E., Hair, J. W., Fenn, M., Shingler, T., Kondragunta, S., Lyapustin, A., Wang, Y., Holben, B., Giles, D. M., and Saide, P. E.: Evaluation and intercomparison of wildfire smoke forecasts from multiple modeling systems for the 2019 Williams Flats fire, Atmospheric Chemistry and Physics, 21, 14427–14469, https://doi.org/10.5194/acp-21-14427-2021, 2021.

https://doi.org/10.5194/essd-2025-427
Preprint. Discussion started: 27 December 2025

Yuan, Z., Wu, D., Wang, T., Ma, X., Li, Y., Shao, S., Zhang, Y., and Zhou, A.: Holocene fire history in southwestern China linked to climate change and human activities, Quaternary Science Reviews, 289, 107615, https://doi.org/10.1016/j.quascirev.2022.107615, 2022.

Zhao, H., Yang, G., Tong, D. Q., Zhang, X., Xiu, A., and Zhang, S.: Interannual and seasonal variability of greenhouse gases and aerosol emissions from biomass burning in northeastern China constrained by satellite observations, Remote Sensing, 13, 1005, https://doi.org/10.3390/rs13051005, 2021.

Zhou, Y., Xing, X., Lang, J., Chen, D., Cheng, S., Wei, L., Wei, X., and Liu, C.: A comprehensive biomass burning emission inventory with high spatial and temporal resolution in China, Atmospheric Chemistry and Physics, 2839–2864, https://doi.org/10.5194/acp-17-2839-2017, 2017.

Zong, Z., Wang, X., Tian, C., Chen, Y., Qu, L., Ji, L., Zhi, G., Li, J., and Zhang, G.: Source apportionment of $PM_{2.5}$ at a regional background site in North China using PMF linked with radiocarbon analysis: insight into the contribution of biomass burning, Atmospheric Chemistry and Physics, 16, 11249–11265, https://doi.org/10.5194/acp-16-11249-2016, 2016.